Open-Slot Antenna Integrated in the Ceramic Head of a Ti-13Nb-13Zr Hip Implant

Mehmet Emre Korkmaz, *Student Member, IEEE*, Wulf Wulff, Thomas-Martin Schuldt, *Member, IEEE* and Sema Dumanli, *Senior Member, IEEE*

***Abstract*—Wireless links between implants and external systems require carefully designed antennas due to strong electromagnetic losses and detuning effects in biological tissues. This work presents the design and analysis of an open-slot antenna integrated into an instrumented orthopedic hip implant for real-time wireless telemetry. The antenna is located inside the modular ceramic head of a Ti-13Nb-13Zr alloy-based implant, establishing wireless communication while preserving the mechanical and antimicrobial properties of the titanium femoral stem. The proposed design eliminates the need for any surface modification of the metallic implant, maintaining its integrity and biocompatibility. The antenna operates in the 2.4 GHz Industrial, Scientific, and Medical (ISM) band, supporting Bluetooth Low Energy connectivity. The wireless connection is validated through numerical analysis of the hip implant and surrounding tissues, as well as measurements in physical phantoms. The measurements show that the proposed antenna achieves a -10 dB bandwidth of 119 MHz. The transmission characteristics demonstrate a wireless communication range of up to 75 cm for a transmit power of -20 dBm and a receiver sensitivity of -95 dBm.**

***Index Terms*—slot antennas, implants, biomedical telemetry**

I. Introduction

TOTAL hip replacement (THR) is one of the most commonly performed surgical procedures worldwide [1]. It provides pain relief and improved mobility for patients with degenerative joint diseases, trauma, or congenital conditions. More than 2 million THR surgeries are performed worldwide [2]. In Organisation for Economic Co-operation and Development (OECD) countries, the mean is 191.5 per 100,000 population, and in the US, 326,000 total hip replacement procedures are performed annually [3], [4]. This number is expected to increase substantially in the coming years due to the ageing population and the rising prevalence of osteoarthritis [5]. Even though THR procedures are usually successful, revision surgeries can still be necessary. Approximately 5–10% of implants require revision within 10–15 years due to aseptic loosening, infection, or mechanical wear. These revisions not only increase patient morbidity but also cause substantial economic costs for healthcare systems [6], [7]. To overcome these problems, orthopedic implants equipped with sensors and wireless telemetry have been proposed to provide real-time tracking of the implant and surrounding tissue conditions [8] [9]. These instrumented implants could allow continuous monitoring of strain, mechanical load, early signs of infection, and wear, enabling earlier intervention and personalised treatment. Such systems could improve patient outcomes, reduce the risk of late-stage complications, and lower the health and economic burden of revision surgeries.

For instrumented implants to be acceptable, wireless communication links are required. Several approaches have been utilized to establish such links. Inductive coupling has been used in biomedical devices due to its simplicity and efficiency, but its range and sensitivity to alignment limit its practicality for larger and deeper implants [10]. Radio-frequency (RF) telemetry has emerged as a common strategy. It offers higher data rates, standardized frequency allocations such as the Medical Implant Communication System (MICS) (402–405 MHz) and Industrial, Scientific, and Medical (ISM) (2.4–2.5 GHz) bands, and greater flexibility in system integration [11] [12] [13] [14] [15] [16]. For this study, an antenna that forms wireless communication using the Bluetooth Low Energy standards is designed. The operating frequency of 2.45 GHz is chosen due to its near-optimal tradeoff between implant antenna efficiency, which is lowered due to high level of miniaturization in lower frequencies, and absorption losses in biological media, which increase at higher frequencies. 2.45 GHz offers a favorable balance for this implant depth, enabling a compact antenna design with acceptable link budget [17]. Despite RF-based telemetry being promising, it remains challenging. The high permittivity and conductivity of tissues cause strong dielectric loading and absorption losses. The variability of the surroundings of the antenna due to movement and healing cause detuning and change in antenna performance. These factors limit radiation efficiency and complicate link establishment. Therefore, an efficient implantable antenna with compact size is a critical requirement for wireless orthopedic systems.

This work presents an antenna design developed within the framework of a multidisciplinary initiative involving collaboration between universities and industrial partners across Europe. The project aims to develop an orthopedic hip implant incorporating sensors that allow the real-time wireless monitoring of strain, acceleration, and temperature. Furthermore, the

Manuscript received October 31, 2025. This work was supported by TÜBİTAK International Research Activities by Small and Medium-Sized Enterprises (IraSME) under the collaborative project DIAMOND (Grant No. 221N271), entitled "Development of Intelligent and Advanced Implants Made of Nanostructured Ti-13Nb-13Zr Alloy (DIAMOND)," with collaboration between academic and industrial partners across Europe, including Boğaziçi University, the Technical University of Darmstadt (PtU), the Technical University of Braunschweig (IfW), the Medical University of Innsbruck, ADVANTIQX, ME-Meßsysteme GmbH, EO-SOL GmbH, and TST Medical Devices Ltd. *Corresponding author: Sema Dumanli.*

M. E. Korkmaz and S. Dumanli are with the Department of Electrical and Electronics Engineering, Boğaziçi University, İstanbul, 34343 Turkey (e-mail: mehmet.korkmaz@bogazici.edu.tr; sema.dumanli@bogazici.edu.tr).

W. Wulff and T. M. Schuldt are with ME-Meßsysteme GmbH Eduard-Maurer-Str. 9 DE-16761 Hennigsdorf, Germany (e-mail: w.wulff@me-systeme.de; t.schuldt@me-systeme.de)

implant is developed using the titanium alloy Ti-13Nb-13Zr (TNZ), which avoids cytotoxic elements such as aluminium and vanadium while providing a lower elastic modulus and superior biocompatibility [18] [19].

Antenna placement and design within orthopedic implants are restricted by both electromagnetic and biological requirements. The outer surface of the hip implant is specifically engineered to provide antimicrobial functionality and promote long-term bone integration. Because any modification of this surface would compromise its biomechanical integrity and antimicrobial performance, it must remain undisturbed and unaltered. Therefore, the antenna cannot be positioned on or near the outer surface but must be fully integrated within the implant body. The other parts being conductive, the ceramic modular head offers the only suitable place for antenna integration due to its dielectric properties. The ceramic head sits on the neck of the hip implant which is secured during the operation. Therefore, the antenna cannot be located under the ceramic head due to mechanical reasons. Similarly, the antenna cannot be located on the ceramic head since the acetabular cup sits on the ceramic head and it is a movable part. Therefore, we propose to have a double layered ceramic head which consists of two interlocking parts and contains the antenna between them. The antenna's isolated position within the ceramic head reduces the risk of detuning due to tissue loading as well as resolving bio-compatibility issues. The antenna embedded in the ceramic head is connected to the sensor and transceiver system located in the neck of the hip implant, ensuring a robust and compact solution for sensing and communication.

In this paper, the design and implementation of an open-slot antenna for a hip implant are presented. The antenna is based on an open-slot configuration. Antenna design and prototyping are presented, and system-level measurements are performed. The test set-up consists of a solid bone phantom merged in muscle phantom, and a total hip implant secured in the bone phantom as it would be done in a hip replacement surgery. The hip implant is jointly developed by the project partners, consists of the TNZ stem, double-layered ceramic head micro-machined for the connection to the antenna, and a generic acetabular cup of stainless steel as seen in Fig. 1. Measurements are conducted in an anechoic chamber with a turntable. Section II explains the antenna model. The methodology is presented in Section III with numerical and experimental setups. Input and transmission responses are discussed in Section IV with a realistic link assessment. Lastly, the conclusion is given in Section V.

II. Antenna Model

The orthopedic hip implant used in our design consists of a Ti-alloy femoral stem, a modular ceramic head, a polyethylene terephthalate (PET) insert, and a Ti-alloy acetabular cup. The ceramic head of the hip implant is designed as a two-layer structure, consisting of two concentric hemispherical shells with an air gap in between, as seen in Fig. 1. The proposed implant antenna is located at the bottom of this gap. A dome-shaped air cavity with a radius of curvature of 11.4 mm and a height of 3.6 mm is left above the antenna. The dome

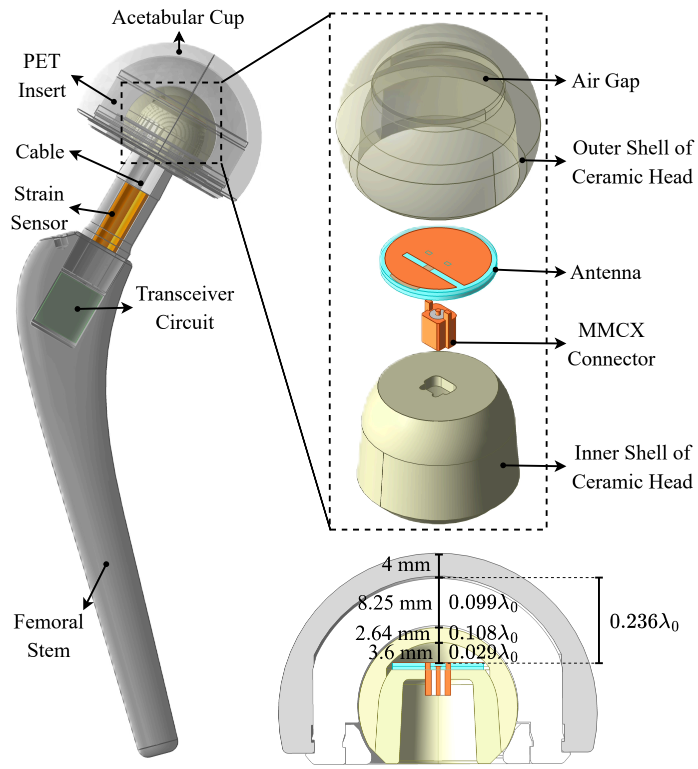

Fig. 1. The hip implant model with exploded view of inside the ceramic head and cross section of the ceramic head with dimensions.

coincides with the antenna's circular edges, and the upper surface of the antenna forms the base of this dome. The antenna is a $\frac{\lambda}{4}$ open-slot antenna as seen in Fig. 2 and it is designed on Rogers RO3210 with a relative permittivity of 10.2 [20]. According to the magnetoelectric duality principle, the proposed open-slot antenna can be considered equivalent to an electric monopole antenna [21]. The slot length of the antenna should be $\frac{\lambda_{\text{eff}}}{4}$ instead of $\frac{\lambda_{\text{eff}}}{2}$ based on image theory [22]. $\epsilon_{\text{r,eff}}$ can be calculated using (1).

$$\epsilon_{\text{r,eff}} = \epsilon_{\text{r,below}} \times ff + \epsilon_{\text{r,above}} \times (1 - ff). \quad (1)$$

The filling factor (ff) can be taken as 50% which is a typical value for co-planar waveguides. $\epsilon_{\text{r,below}}$ is 10.2, the relative permittivity of the substrate. If $\epsilon_{\text{r,above}}$ is taken as 1, $\epsilon_{\text{r,eff}}$ is calculated to be 5.6. However, $\epsilon_{\text{r,above}}$ must be greater than 1 because the air layer is encapsulated with the ceramic layer. Hence, $\epsilon_{\text{r,eff}}$ of the slot should be greater than the calculated value of 5.6. When $\epsilon_{\text{r,eff}}$ is calculated by reverse engineering from the simulated slot length and its corresponding frequency, $\epsilon_{\text{r,eff}}$ is found to be 6.6 which aligns with the equation's estimation [23].

The antenna is fed with a top-loaded microstrip line, which is designed on an additional layer of RO3210 to avoid direct contact with the high-permittivity (ϵ_r = 26) ceramic head, ensuring that the feed line remains relatively wide for ease of manufacturing. Due to the implant geometry and the RF transceiver placement, it is best to feed the antenna centrally and perpendicular to the titanium neck of the hip implant.

Therefore, the slot is located at an offset relative to the ground plane.

Finally, the acetabular cup is used as a reflector so that the propagation direction ensures off-body transmission. The outer shell of the ceramic head with a thickness of 2.64 mm (electrical length=0.108 λ_0) is located 3.6 mm (0.029 λ_0) from the antenna. A PET insert with a thickness of 8.25 mm (0.099 λ_0) fills the gap between the ceramic head and the Ti-alloy acetabular cup, which has a thickness of 4 mm. Therefore, the total distance from the radiator of the antenna to the Ti-alloy acetabular cup sums up to $0.236 \times \lambda_0$ which is approximately a quarter wavelength.

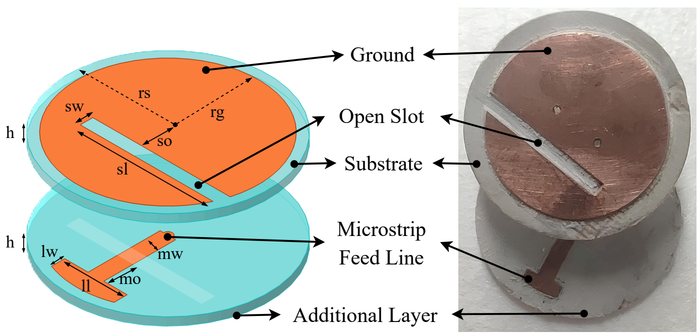

(a) (b)

Fig. 2. The exploded view of the implant antenna (a) simulation model (b) fabricated antenna where sl = 10.75 mm, sw = 1 mm, so = 2 mm, mo = 3.25 mm, mw = 1.25 mm, ll = 3 mm, lw = 1mm, rs = 8 mm, rg = 7.25 mm, and h = 0.64 mm.

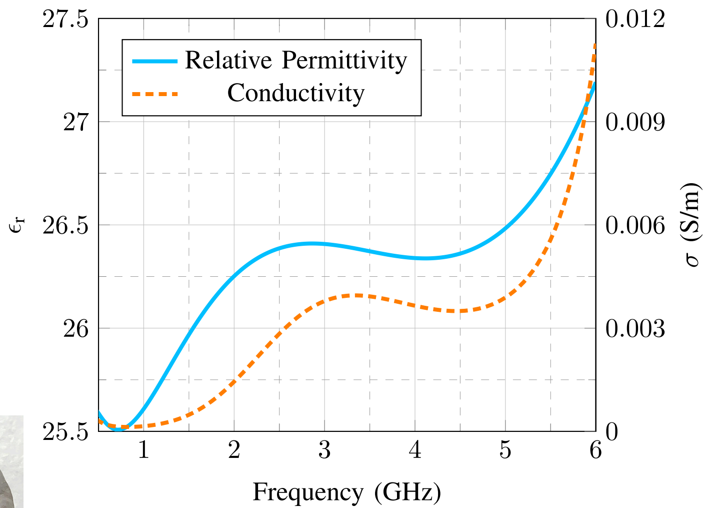

Fig. 3. The relative permittivity and conductivity values of the ceramic material used in the implant.

III. Methodology

A. Numerical Set-up

To evaluate the electromagnetic performance of the implant antenna, a 3D model of the hip implant is constructed with its components: the Ti-alloy femoral stem, ceramic modular head, PET insert, and Ti-alloy acetabular cup. The open-slot antenna is positioned inside the ceramic modular head as previously described. The Ti-alloy parts are modeled with an electrical conductivity of 1820000 S/m and the dielectric properties of the ceramic material employed are measured using the SPEAG DAK-3.5-TL2 probe, and presented in Fig. 3 [24].

The antenna and hip implant are located inside the ANSYS Human Body Phantom with a resolution of 2 mm [25]. To reduce the computational cost of the simulations, the phantom model is physically modified to include only the relevant region between the hip and the knee which still preserves the anatomical fidelity required for accurate wave propagation analysis as seen in Fig. 4. The numerical phantom consists of two different frequency dependent material definitions: human muscle and human bone cortical.

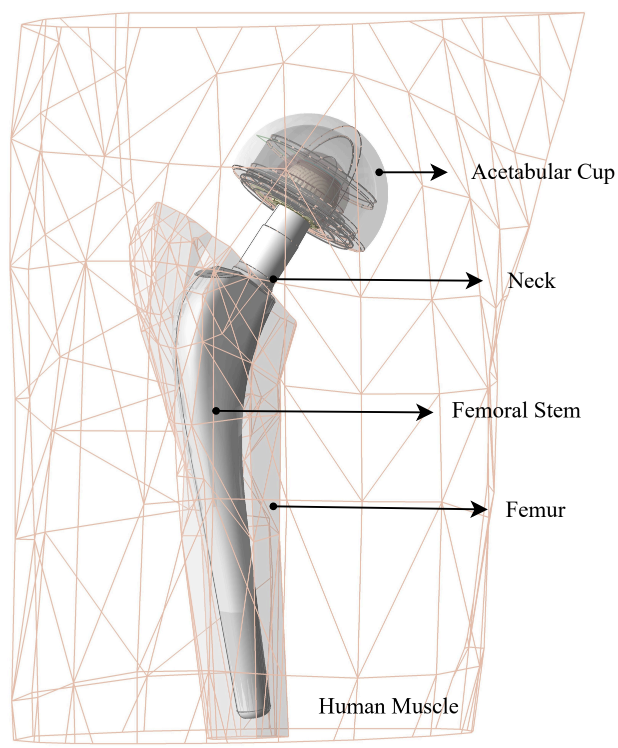

Fig. 4. The simulation model for the implant antenna located inside the hip implant.

B. Experimental Set-up

A measurement setup is designed to emulate an anatomical configuration and to provide a stable and repeatable antenna characterization, as illustrated in Fig. 5. A 3D-printed leg-shaped container accommodates the muscle phantom, the bone phantom, and the orthopedic implant assembly. The implant system consists of the TNZ femoral stem and neck, the modular ceramic head embedding the proposed antenna, the PET insert, and a generic stainless steel acetabular cup.

The container is mounted on a manually rotatable 3D-printed turntable supported by glass marbles to minimize friction and maintain stability during measurements. Angular indicators at 10° increments are integrated into the turntable, allowing precise and repeatable positioning of the implant with respect to the reader antenna.

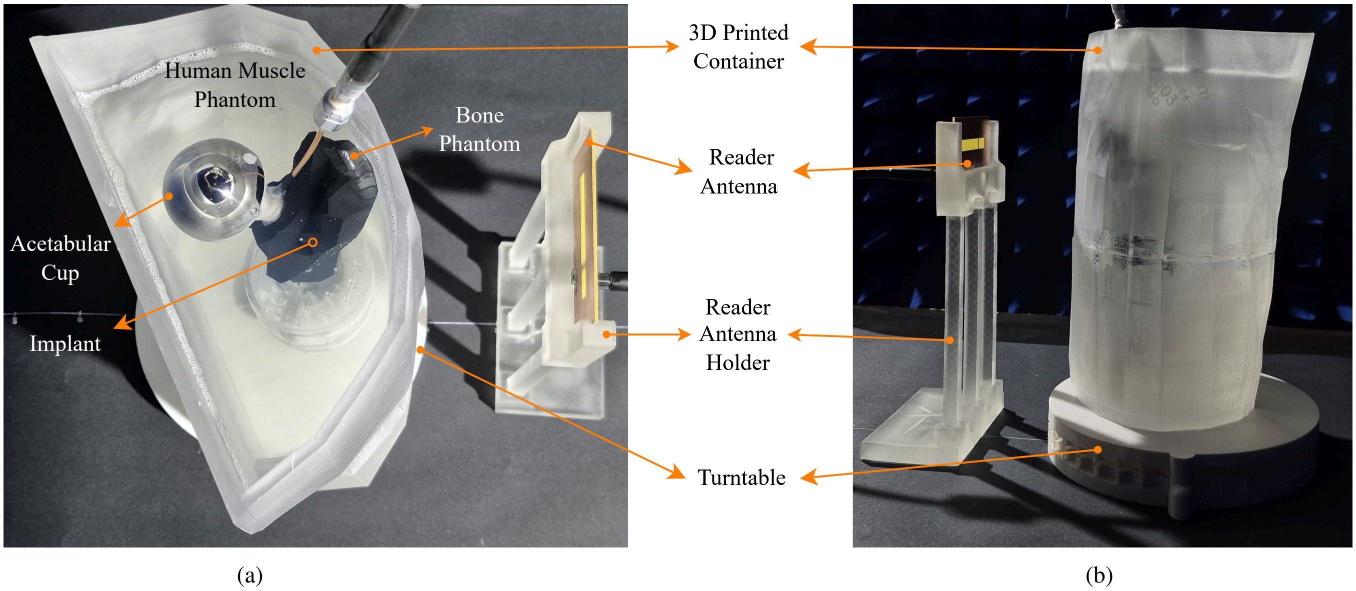

Fig. 5. The measurement setup for both input and transmission response measurements. (a) Top view (b) side view.

A conventional slot antenna with overall dimensions of 90 × 40 × 1.57 mm, incorporating a 60 × 8 mm slot, is employed as the off-body reader. It operates in the 2.4 GHz ISM band, as shown in Fig. 6. The antenna is fed via a microstrip line.

The origin of the coordinate system is located at the center of the implant antenna. The Z-axis centers of the implant and reader antennas are aligned. The distance R and angle Φ in cylindrical coordinates define the radial and angular position of the reader antenna, respectively, as shown in Fig. 7. For the radiated power analysis, first, R is kept constant while the Z-center and Φ are changed. Then the Z-center of the reader antenna is kept constant while R and Φ are varied. Z-axis adjustments are achieved using modular spacers, each providing a 1 cm of elevation. The holder ensures stable vertical adjustment.

Measurements are performed using a Rohde & Schwarz ZNLE6 vector network analyzer (VNA) [26]. Ferrite rings are placed along the coaxial cables to suppress the effect of the cable for the implant antenna and a rotary joint is employed to allow smooth rotation of the implant antenna connection during measurements. A Through-Open-Short-Match (TOSM) calibration is carried out prior to each set of measurements. The calibration plane is extended to both the reader antenna port and the implant antenna port to ensure accurate acquisition of the S parameter.

1) Muscle Phantom: To mimic the electromagnetic properties of human muscle tissue for experimental validation, a liquid phantom is developed using Triton X-100, distilled water, and NaCl as listed in Table I [27] [28]. 1.177 kilograms of Triton X-100 is preheated to 45 °C in a water bath. The 3.878 kilograms of water is mixed with the 26.9 grams of NaCl and preheated to 45 °C as well. After both reached 45 ° C, they are mixed together and stirred with a magnetic stirrer until homogeneous. The dielectric properties of the prepared muscle phantom are measured using a SPEAG DAKS 3.5 probe as plotted in Fig. 8 [29]. The phantom has a relative permittivity

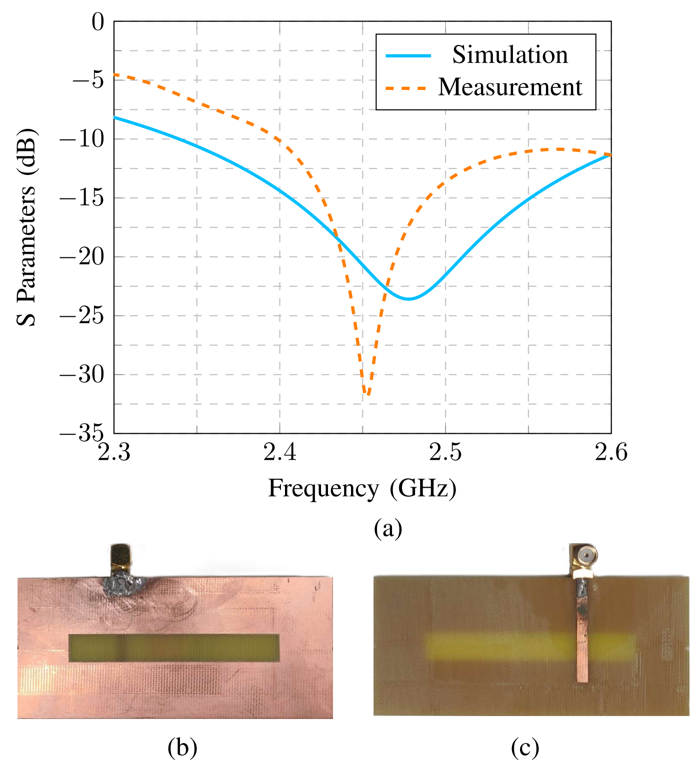

Fig. 6. (a) The simulated and measured reflection coefficients for the off-body reader slot antenna. (b) Front and (c) back view of the fabricated antenna.

of 52.5 and a conductivity of 1.75 S/m at 2.45 GHz. Hence, the error from the real tissue is 0.38% for permittivity and 0.57% for conductivity.

2) Bone Phantom: To emulate the dielectric properties of human cortical bone, a femur-shaped phantom is fabricated using RTV-2 silicone as the polymer matrix with graphite and carbon black fillers. The mixture is prepared by combining 10 g of RTV-2 silicone, 1.5 g of graphite powder, and 0.25

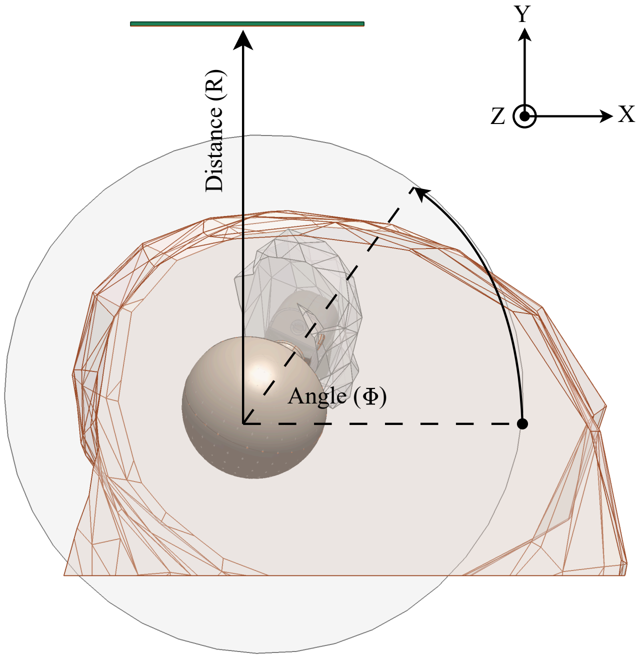

Fig. 7. The annotated visual sketch of the measurement setup for transmission response measurements.

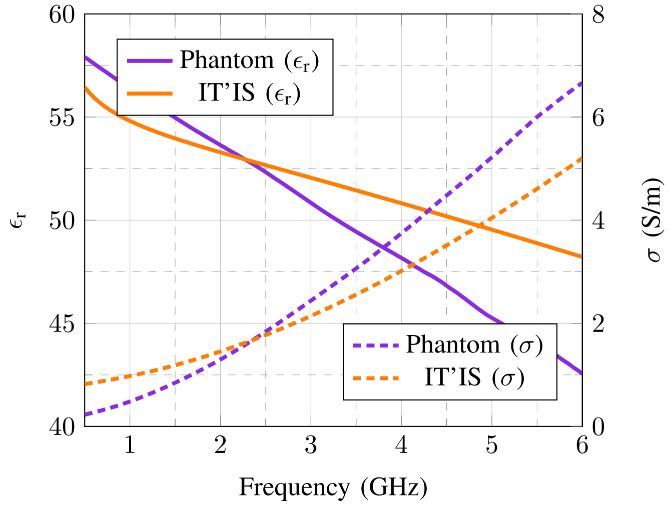

Fig. 8. The relative permittivity and conductivity values of the human muscle phantom compared to the literature [31] [32].

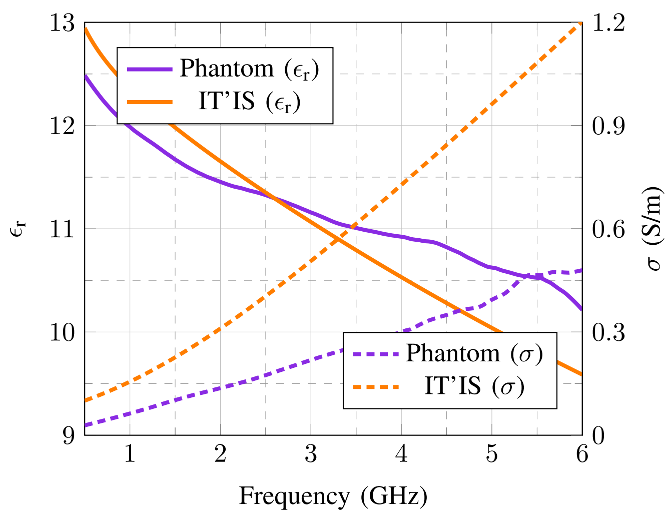

Fig. 9. The relative permittivity and conductivity values of the human cortical bone phantom compared to the literature [31] [32].

g of carbon black, as listed in Table I [30]. After thorough mixing, the composite is poured into a life-size femur mold produced via SLA 3D printing, degassed in a vacuum oven, and cured at room temperature for 24 hours. The dielectric properties of the prepared bone phantom are measured using a SPEAG DAKS 3.5 probe, as shown in Fig. 9. The phantom exhibits a relative permittivity of 11.3 and a conductivity of 0.17 S/m at 2.45 GHz. The target values are 11.4 and 0.39, respectively, showing good agreement for the relative permittivity. However, the conductivity value is lower than the target. Achieving a higher conductivity requires a higher carbon black filler content, which increases the viscosity of the mixture and therefore makes it difficult to remove trapped air bubbles. As a result, achieving a moldable and homogeneous phantom becomes progressively more challenging. Therefore, the simulations are repeated with a lower-conductivity numerical bone phantom. This results in the transmission coefficient (S_{21}) between the implant and reader antenna deviating by less than 1 dB, while the reflection coefficient (S_{11}) remains unchanged. Consequently, the bone phantom is regarded as acceptable for measurements.

TABLE I
COMPOSITION OF THE MUSCLE TISSUE-MIMICKING PHANTOM AND THE BONE TISSUE-MIMICKING PHANTOM

Muscle		Bone	
Triton	1.177 kg	RTV-Silicon	10 g
Water	3.878 kg	Graphite	1.5 g
NaCl	26.9 g	Carbon Black	0.25 g

C. Implant Assembly

The assembly of the implant used for measurements is shown in Fig. 10. This configuration closely follows the concept design presented in Fig. 1. The prototyped antenna is placed onto the ceramic core, with the MMCX connector fitted into its preallocated, shaped cavity within the core. The ceramic cap is then positioned on top of the antenna–ceramic core assembly, together forming the ceramic head. The antenna inside the ceramic head is connected to the transceiver circuit through a micro-coaxial (MMCX–U.fl) cable that passes through the titanium neck of the hip implant. The ceramic core is mounted onto the titanium neck of the hip implant, which in turn is inserted into the titanium stem. Finally, the titanium acetabular cup with a PET insert is attached to enclose the ceramic core. The fully assembled implant is positioned within

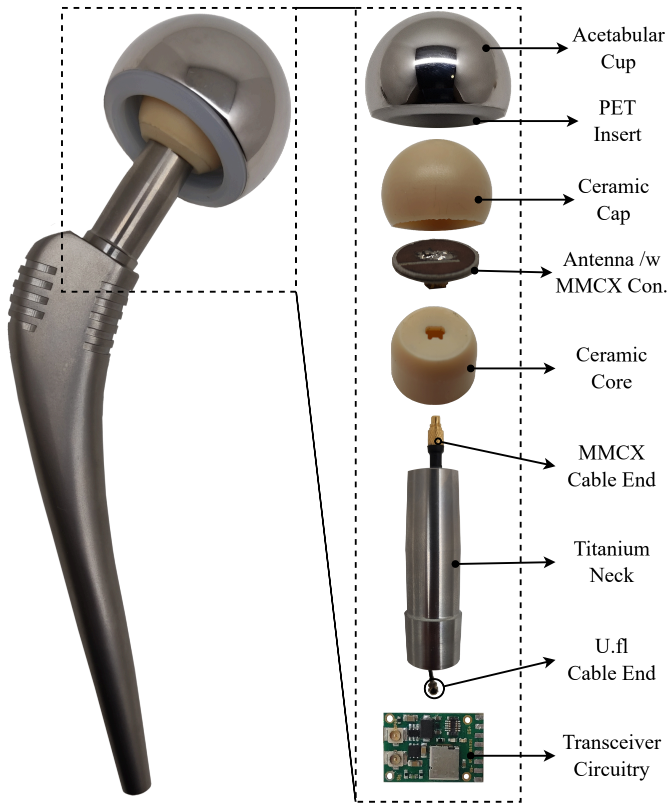

Fig. 10. The assembly steps of the implant

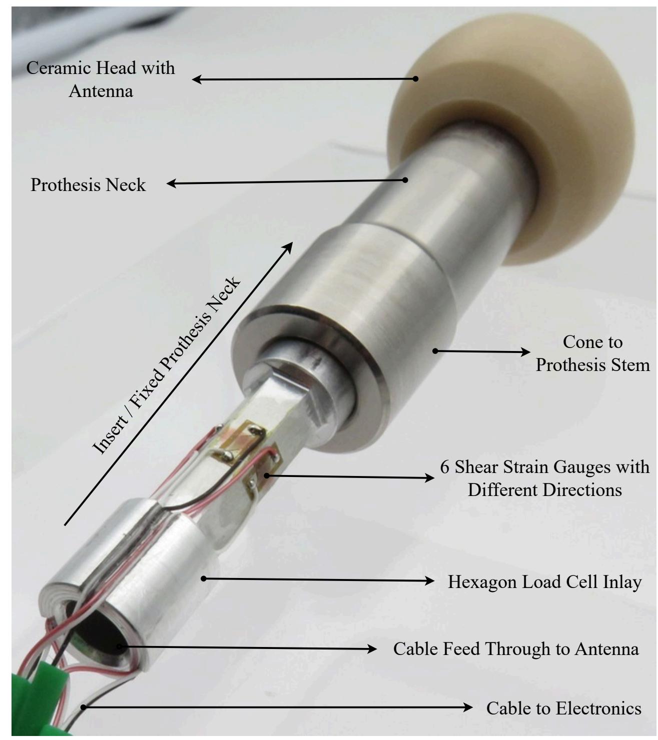

Fig. 11. The instrumentation of the neck of the hip implant with shear strain gauges.

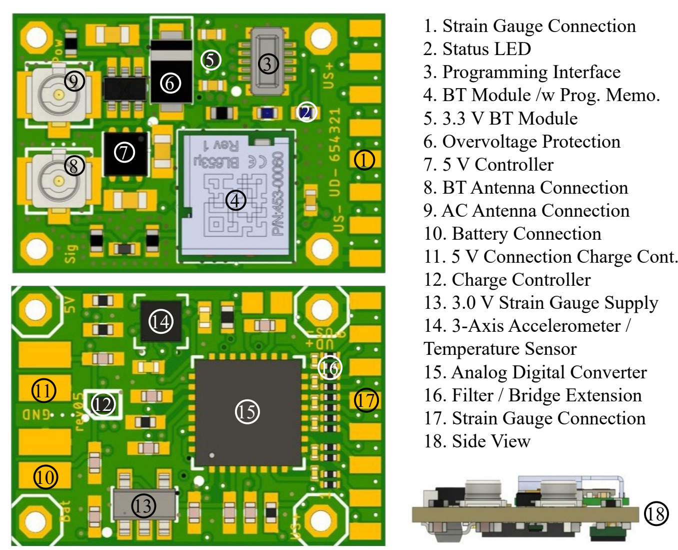

Fig. 12. The component layout and pin-out of the wireless sensor module.

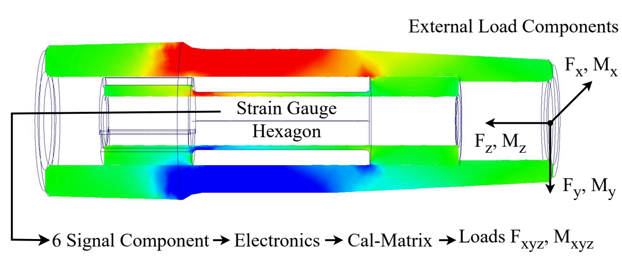

Fig. 13. The neck of the hip implant with load cell inlay.

the bone phantom, which is then placed inside a 3D-printed container filled with human muscle phantom, as illustrated in Fig. 5.

D. Transceiver and Sensor Architecture

The measurement technology integrated within the hip implant is divided into two primary components: the hexagonal measuring cell, shown in Fig. 11, and the sensor–transceiver electronics that include temperature and three-axis acceleration sensors, shown in Fig. 12. The hexagonal measuring cell is positioned in the neck region of the hip implant, while the electronic module is located directly below it within its stem, as shown in Fig. 10.

In the electronic subsystem, the analog signals obtained from the six-axis load cell are amplified, processed, digitized, and transmitted through a Bluetooth module, which also collects data from the temperature and acceleration sensors. The antenna signal is conveyed through a coaxial cable passing along the central bore of the hexagonal measuring cell to the antenna embedded in the femoral head.

The function of the six-axis hexagonal measuring cell is based on six individual shear strain gauges arranged in distinct orientations, as depicted in Fig. 13. Each gauge produces an independent analog signal corresponding to a specific load direction. These six raw signals are subsequently converted into three forces and three moments by means of a 6×6 calibration matrix stored in the microcontroller memory of the Bluetooth (BT) module, as shown in Fig. 12. The matrix is derived during calibration and relates the Cartesian load components (F_x, F_y, F_z, M_x, M_y, M_z) to the corresponding strain-gauge outputs (Q). During operation, the microcontroller computes the resultant load vector F_T by multiplying the signal vector Q with the calibration matrix M, i.e., $F_T = Q \times M$.

Each instrumented implant is required to be calibrated and programmed prior to implantation to ensure accurate operation. Power will be supplied by a rechargeable battery located below the electronics within the stem.

IV. Results

A. Input Response

The simulated and measured reflection coefficients of the implant antenna are given in Fig. 14. The implant antenna operates in the 2.4 GHz ISM band. The measured results demonstrate agreement with the simulations and confirm that the proposed implant antenna, when embedded within the ceramic head, maintains sufficient bandwidth for reliable Bluetooth communication.

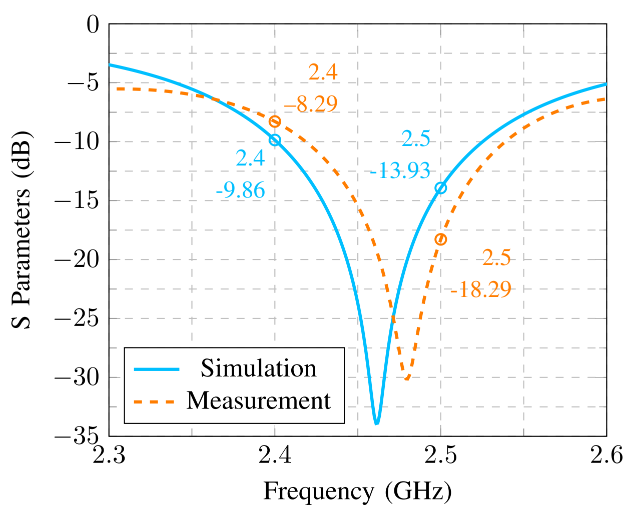

Fig. 14. The simulated and the measured reflection coefficients for the implant antenna.

B. Transmission Response

The power radiated from the implant antenna is assessed through simulations and measurements at different angles, elevations, and radial distances.

1) Simulated Results: Since the antenna is embedded within biological tissue, conventional antenna characteristics such as the far-field radiation pattern are not directly meaningful. Unlike antennas operating in free space, implant antennas radiate into a lossy medium where the near field strongly couples with the surrounding tissues, resulting in increased power loss. This strong near-field coupling with lossy tissues is one of the primary reasons for the low radiation efficiency of implanted antennas. Once the electromagnetic waves leave the reactive near-field region, they propagate through the surrounding biological tissues and experience attenuation along their transmission path. This attenuation, referred to as propagation loss, is significantly higher than the free-space path loss due to the lossy nature of biological tissues. As the waves reach the boundary between the body and free space, the discontinuity in electromagnetic properties between the two media causes reflections, leading to additional power loss. Consequently, the radiation characteristics of implant antennas depend not only on the antenna structure itself but also on the shape, dimensions, and electromagnetic properties of the surrounding biological tissues. As a result, the radiation pattern of an implant antenna becomes highly dependent on the medium, the choice of the coordinate system, and the reference origin [33] [34] [35]. Therefore, to evaluate the radiation performance of an implant antenna, it is often more appropriate to analyze the amount of power that reaches outside the body. In this context, the total radiated power serves as a meaningful figure of merit. Accordingly, Fig. 15 presents the total radiated power passing through a surface with dimensions identical to those of the reader antenna used in the measurement setup. To generate a heatmap, R is set to 15 cm. Φ is swept between $0°$ and $180°$ with $10°$ steps. Z center of the surface is varied between -2 cm and 4 cm with 1 cm steps. The simulations predict that the received power is -38.3 dBm and -62.9 dBm for the best and worst case scenarios with a transmit power level of 10 dBm.

In addition to the communication link performance, the safety of the implant antenna operation is also assessed through specific absorption rate (SAR) analysis. The maximum SAR value is found to be 0.392 W/kg averaged over 10 g of tissue, which is adequately below the safety limit of 2.0 W/kg.

2) Measurement Results: The implant antenna is measured using the previously mentioned measurement setup with a turntable mechanism and an off-body reader antenna. The visual representation of the measurement is given in Fig. 7. The distance R between the implant antenna and the off-body reader antenna is kept at 15 cm during measurements. Because the phantom is shaped like a human leg, the in-body and air distances vary with the angle. For $\Phi = 0$ and $Z = 0$, the in-body distance of 75 mm equals the distance in air. Fig. 16 shows the S_{21} between the implant antenna and the off-body reader antenna as Φ is swept between $0°$ and $180°$ with $10°$ steps and -2 to +4 cm of Z-axis adjustments of the reader antenna. To emulate the Bluetooth Low Energy (BLE) standard, which uses adaptive frequency hopping (AFH), the maximum S_{21} value detected within the 2.4 GHz ISM band is chosen for the plot. As seen in the heatmap, the maximum and minimum received transmission coefficients for all elevations and angles are -56.8 dB and -73.4 dB, respectively. The maximum S_{21} is observed at $\Phi = 140$ which is shifted from the expected angle predicted by simulations. This is thought to be because of measurement inaccuracies related to the tilt angle of the femur in the setup.

The transmit power level of the implant transceiver can be set between -20 dBm and 4 dBm, and the sensitivity of BLE receivers ranges between -95 dBm and -105 dBm. Considering the worst-case scenario of -20 dBm transmit power and -95 dBm sensitivity, even at the greatest elevation of 4 cm and the worst angular position, a reliable connection can still be secured at 15 cm. If the mobile device is vertically aligned with the implant and located at the best angle according to

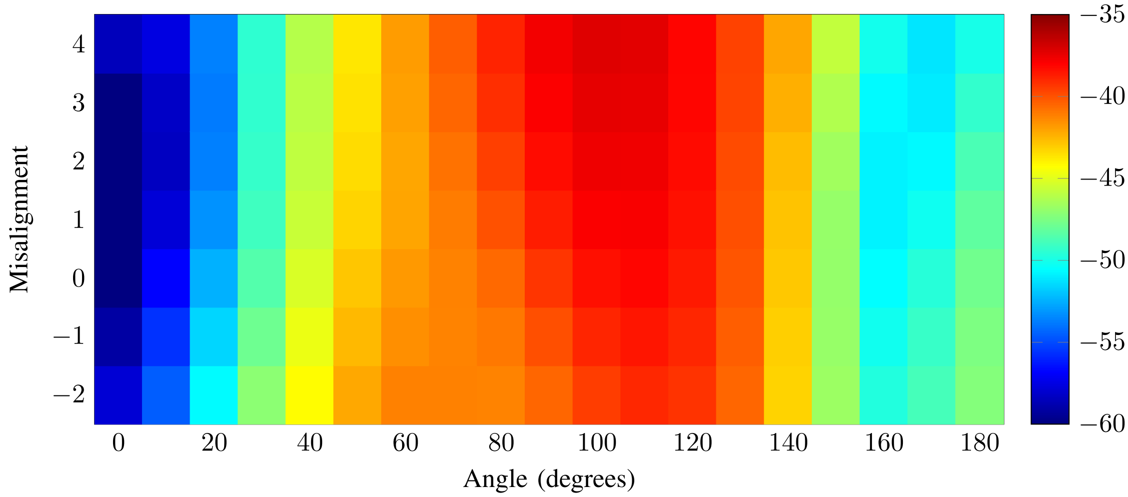

Fig. 15. The heatmap of the received power values on a 90 mm x 40 mm surface for varying Z and Φ values. The received power is plotted in dBm for a transmit power level of 10 dBm.

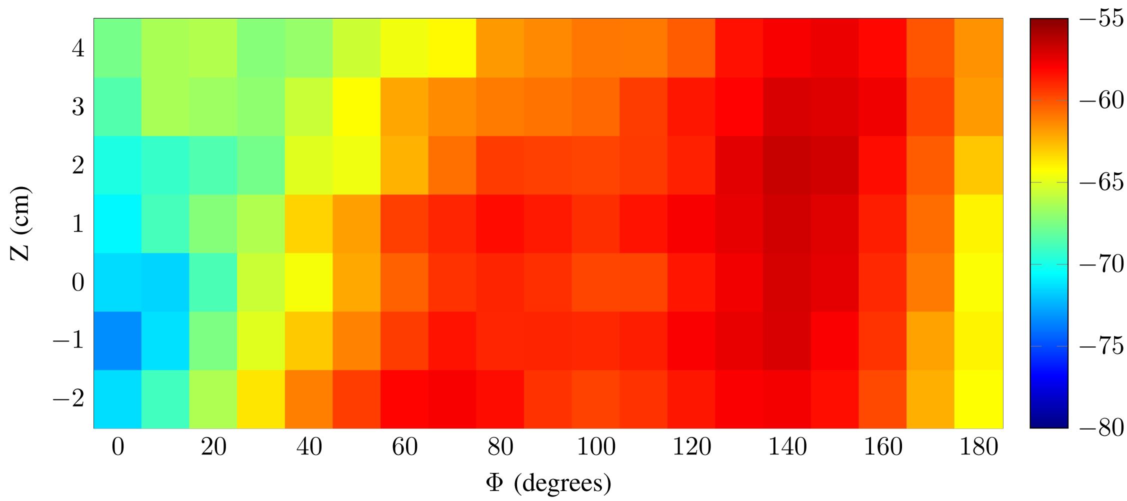

Fig. 16. The heatmap of the transmission coefficient values (dB) between the implant and the off-body reader antennas for varying Z and Φ values.

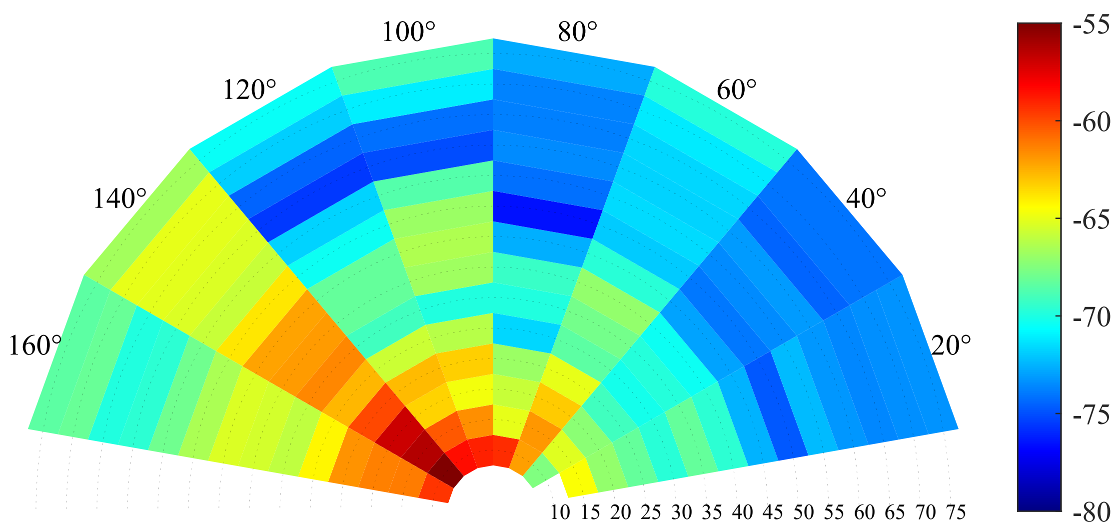

Fig. 17. The semi-circular heatmap of the transmission coefficient values (dB) between the implant and the off-body reader antennas for for varying R and Φ values.

the human body, there is 52.2 dB to spare towards path loss for the best case transmit power and sensitivity pairing which translates to approximately 4 m range.

To evaluate the communication range of the implant antenna, the transmission coefficient (S_{21}) is measured as Φ is swept between 20° and 160° with 10° steps and R is varied between 10 to 75 cm with 5 cm steps as seen in Fig. 17. The reader antenna is positioned at $Z = 2$ cm and kept the same during measurements. Considering -20 dBm implant transmit power level and -95 dBm BLE receiver sensitivity, which is the worst case scenario, the analysis shows that the proposed antenna supports a reliable BLE link up to 75 cm for all angles.

C. A Realistic Link

To validate the performance of the wireless link, a more realistic scenario is emulated where the implant inside the phantom is connected to a laptop. The antenna is connected to the sensor–transceiver circuitry, as illustrated in Fig. 10. The Bluetooth (BT) module is programmed to transmit advertisement packets at the 2.4 GHz band at regular intervals. As shown in Fig. 18, a laptop equipped with a commercial Bluetooth chip is used as the receiver, and the connection is tested at various angles and distances from the implant. During testing, the communication range varied up to 75 cm, with no packet loss observed. The measured performance aligns well with the S_{21}-based range analysis presented in Section IV-B and Fig. 17, which highlights the dependence of transmission efficiency on both distance and angular alignment relative to the implant.

These BLE measurement results confirm that the proposed open-slot implant antenna can sustain a stable and reliable wireless communication link through tissue-equivalent environments. The findings demonstrate the antenna's compatibility with Bluetooth protocols and its suitability for integration into instrumented orthopedic implants that require real-time data telemetry.

V. Conclusion

In this work, an open-slot antenna has been proposed to establish a wireless link for an instrumented hip implant equipped with sensors. The antenna is positioned between the two interlocking parts of the modular ceramic head of the hip implant in order to preserve the antimicrobial properties of the Ti-alloy femoral stem, while the Ti-alloy acetabular cup is exploited as a reflector to enhance the transmission performance of the implant antenna. The antenna operates in the 2.4 GHz ISM band, and the transmission coefficient between the implant antenna at a depth of approximately 8 cm and an off-body reader antenna located 15 cm away from the human body is around -55 dB in the best case scenario. The wireless link has been evaluated under different angles, distances, and elevations, demonstrating that a stable wireless connection can be sustained up to around 75 cm within a coverage angle of approximately 140° for a transmit power of -20 dBm and a receiver sensitivity of -95 dBm. Under more realistic operating conditions, the maximum range for a stable wireless connection varies from 50 cm to 75 cm. Therefore, this link ensures reliable communication performance between the implant and the outside world.

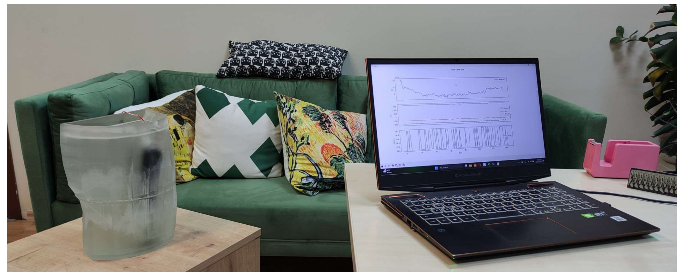

(a)

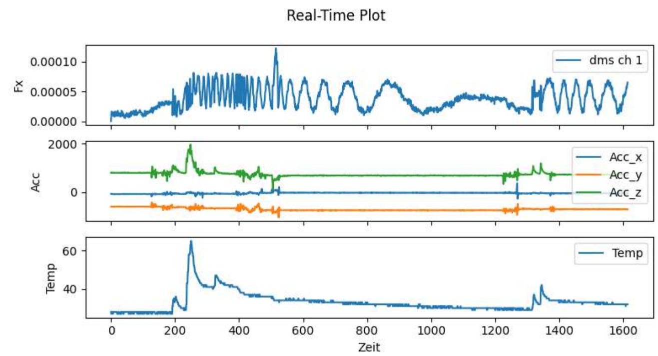

(b)

Fig. 18. (a) Measurement setup for testing the communication link between the implant and a laptop receiver and (b) the interface displaying the sensor data received from the implant.

Acknowledgment

This work was supported by TUBITAK International research activities by small and medium-sized enterprises (IraSME) as part of the DIAMOND project under grant number 221N271. Furthermore, the authors would like to thank our project partners, Dr. Johannes Scherer from ADVANTIQX, Thomas Schuldt from ME-Meßsysteme GmbH, David Putzer from EO-SOL GmbH, and Mehmet Orcun Polat and Gokcan Cinar from TST Medical Devices Ltd., for their support.

References

[1] OECD (2023), Health at a Glance 2023: OECD Indicators, OECD Publishing, Paris, https://doi.org/10.1787/7a7afb35-en.

[2] J. L. Günsche, V. Pilz, T. Hanstein, and R. Skripitz, "The variation of arthroplasty procedures in the OECD Countries: analysis of possible influencing factors by linear regression," Orthopedic Reviews, vol. 12, no. 3, Nov. 2020, doi: https://doi.org/10.4081/or.2020.8526.

[3] T. Jennison, A. MacGregor, and A. Goldberg, "Hip arthroplasty practice across the Organisation for Economic Co-operation and Development (OECD) over the last decade," Annals of The Royal College of Surgeons of England, vol. 105, no. 7, pp. 645–652, Sep. 2023.

[4] Wolford ML, Palso K, Bercovitz A. Hospitalization for total hip replacement among inpatients aged 45 and over: United States, 2000–2010. NCHS data brief, no 186. Hyattsville, MD: National Center for Health Statistics. 2015.

[5] Sloan, Matthew MD, MS; Premkumar, Ajay MD, MPH; Sheth, Neil P. MD. Projected Volume of Primary Total Joint Arthroplasty in the U.S., 2014 to 2030. The Journal of Bone and Joint Surgery 100(17):p 1455-1460, September 5, 2018.

[6] S. Yu et al., "Re-revision total hip arthroplasty: Epidemiology and factors associated with outcomes," Journal of Clinical Orthopaedics and Trauma, vol. 11, no. 1, pp. 43–46, Jan. 2020.

[7] A. Patel, G. Pavlou, R. E. Mújica-Mota, and A. D. Toms, "The epidemiology of revision total knee and hip arthroplasty in England and Wales," The Bone & Joint Journal, vol. 97-B, no. 8, pp. 1076–1081, Aug. 2015.

[8] Y. Qiblawey, M. E. H. Chowdhury, F. Musharavati, E. Zalnezhad, A. Khandakar and M. T. Islam, "Instrumented Hip Implant: A Review," in IEEE Sensors Journal, vol. 21, no. 6, pp. 7179-7194, 15 March 2021.

[9] L. Donyaparastlivari and A. Ibrahim, "A smart hip implant with embedded multidirectional sensing and wireless load monitoring for enhanced orthopedic care," Biosensors and Bioelectronics 26, pp. 100648–100648, Jun. 2025.

[10] M. D. Weiss, J. L. Smith and J. Bach, "RF Coupling in a 433-MHz Biotelemetry System for an Artificial Hip," in IEEE Antennas and Wireless Propagation Letters, vol. 8, pp. 916-919, 2009.

[11] Ladislau Matekovits, F. Mir, Gianluca Dassano, and I. Peter, "Deeply Implanted Conformal Antenna for Real-Time Bio-Telemetry Applications," Sensors, vol. 24, no. 4, pp. 1170–1170, Feb. 2024.

[12] D. Nikolayev, A. K. Skrivervik, J. S. Ho, M. Zhadobov and R. Sauleau, "Reconfigurable Dual-Band Capsule-Conformal Antenna Array for In-Body Bioelectronics," in IEEE Transactions on Antennas and Propagation, vol. 70, no. 5, pp. 3749-3761, May 2022.

[13] R. B. Green, M. Hays, M. Mangino and E. Topsakal, "An Anatomical Model for the Simulation and Development of Subcutaneous Implantable Wireless Devices," in IEEE Transactions on Antennas and Propagation, vol. 68, no. 10, pp. 7170-7178, Oct. 2020.

[14] S. Dumanli, "A cornered shallow cavity backed slot antenna suitable for smart hip implants," 2016 10th European Conference on Antennas and Propagation (EuCAP), Davos, Switzerland, 2016, pp. 1-3.

[15] E. Cil and S. Dumanli, "Characterization of an Implanted Antenna inside a 3D Printed Multilayer Hip Phantom," 2019 13th European Conference on Antennas and Propagation (EuCAP), Krakow, Poland, 2019, pp. 1-4.

[16] A. Bilir and S. Dumanli, "In-body Antenna Design for Next Generation Hip Implants," 2023 24th International Conference on Applied Electromagnetics and Communications (ICECOM), Dubrovnik, Croatia, 2023, pp. 1-4.

[17] Í. V. Soares et al., "Wireless Powering for Long-Lasting Deep-Body Bioelectronic Devices: Solutions, limitations, and new technologies [Bioelectromagnetics]," in IEEE Antennas and Propagation Magazine, vol. 67, no. 3, pp. 74-86, June 2025.

[18] L. Kluy, P. Groche, L. Klinge, C. Siemers, and C. Spiegel, "Nanostructuring of the titanium alloy Ti-13Nb-13Zr (NanoTNZ) for osteosynthesis implants by continuous multidirectional swaging," CIRP Journal of Manufacturing Science and Technology, vol. 58, pp. 47–61, Jun. 2025.

[19] L. Klinge, Lukas Kluy, C. Spiegel, C. Siemers, P. Groche, and Débora Coraça-Huber, "Nanostructured Ti-13Nb-13Zr alloy for implant application—material scientific, technological, and biological aspects," Frontiers in bioengineering and biotechnology, vol. 11, Aug. 2023.

[20] "RO3200 TM Series Circuit Materials." Accessed: Aug. 11, 2025. [Online]. Available: https://www.rogerscorp.com/-/media/project/rogerscorp/documents/advanced-electronics-solutions/english/data-sheets/ro3200-series-data-sheet.pdf

[21] X. Zhu, Z. Wang, B. Yu, Z. Dai and D. Li, "A Planar Wideband Unidirectional Open-Slot Antenna," in IEEE Antennas and Wireless Propagation Letters, vol. 22, no. 5, pp. 1159-1163, May 2023.

[22] C. A. Balanis, Antenna Theory: Analysis and Design. John Wiley & Sons, 2016.

[23] E. Cil and S. Dumanli, "The Design of a Reconfigurable Slot Antenna Printed on Glass for Wearable Applications," in IEEE Access, vol. 8, pp. 95417-95423, 2020.

[24] "DAK-TL2 for Dielectric Measurement of Thin Layers and Liquids," Speag.swiss. https://speag.swiss/products/dak/for-dielectric-measurement-of-thin-layers-and-liquids-dak-tl2 (accessed Oct. 29, 2025).

[25] "Ansys HFSS — Ansys Electronics," https://www.ansys.com/products/electronics/ansys-hfss (accessed Oct. 29, 2025).

[26] "R&S ZNLE vector network analyzer," Rohde-schwarz.com. https://www.rohde-schwarz.com/cz/products/test-and-measurement/network-analyzers/rs-znle-vector-network-analyzer_63493-447936.html (accessed Oct. 31, 2025).

[27] "Simulation," Univ-paris-diderot.fr, 2023. https://applis.iut.univ-paris-diderot.fr/CNRS/simulation.php (accessed Aug. 17, 2025).

[28] N. Joachimowicz, B. Duchêne, C. Conessa, and O. Meyer, "Anthropomorphic Breast and Head Phantoms for Microwave Imaging," Diagnostics, vol. 8, no. 4, p. 85, Dec. 2018.

[29] "DAKS, SPEAG, Schmid & Partner Engineering AG," Speag.swiss. https://speag.swiss/products/dak/daks (accessed Oct. 29, 2025).

[30] M. E. Korkmaz, "Wireless Communication System Design for Smart Orthopedic Implants: Antenna Development and Integration", M.Sc. dissertation, Boğaziçi University, 2026.

[31] Baumgartner C, Hasgall PA, Di Gennaro F, Neufeld E, Lloyd B, Gosselin MC, Payne D, Klingenböck A, Kuster N, "IT'IS Database for thermal and electromagnetic parameters of biological tissues," Version 5.0, August 21, 2025.

[32] C. Gabriel. Compilation of the Dielectric Properties of Body Tissues at RF and Microwave Frequencies, Report N.AL/OE-TR- 1996-0037, Occupational and environmental health directorate, Radiofrequency Radiation Division, Brooks Air Force Base, Texas (USA), 1996.

[33] R. Moore, "Effects of a surrounding conducting medium on antenna analysis," in IEEE Transactions on Antennas and Propagation, vol. 11, no. 3, pp. 216-225, May 1963.

[34] A. K. Skrivervik, M. Bosiljevac and Z. Sipus, "Fundamental Limits for Implanted Antennas: Maximum Power Density Reaching Free Space," in IEEE Transactions on Antennas and Propagation, vol. 67, no. 8, pp. 4978-4988, Aug. 2019.

[35] F. Merli, "Implantable antennas for biomedical applications", Ph.D. dissertation, EPFL, 2011.

Mehmet Emre Korkmaz (Student Member, IEEE) received the B.Sc. degree in Electrical and Electronics Engineering from Boğaziçi University, Istanbul, Turkey, in 2023, where he is currently pursuing the M.Sc. degree. He has been a Researcher with the Antennas and Propagation Laboratory (BOUNtenna) since 2022. He has been working as a Research Assistant at Boğaziçi University, Istanbul, since 2024. He is a recipient of the IEEE 2025 Antennas & Propagation Society Eugene F. Knott Pre-Doctoral Research Grant. His research interests include reconfigurable antenna systems, implantable and wearable antennas, and electromagnetic phantom development.

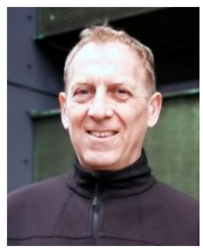

Wulf Wulff (Member, IEEE) received his diploma degree (Dipl.-Ing.) in mechanical engineering and biomedical engineering from the Technische Universität Berlin, Germany, in 2003. He began his professional career with a classic vocational training as a metalworker, which established the foundation for his deep understanding of precision mechanics. He brings over 20 years of experience in biomedical engineering and automation, including positions at the Fraunhofer IPK, the Technische Universität Berlin, the BTU Cottbus-Senftenberg, and as a team leader at Ottobock. Currently, Mr. Wulff is a Senior Development Engineer for force-torque sensors. His primary innovation focus is on the development of sensor technology, among others, applications for biomedical engineering. His most recent scientific breakthrough includes the development of a 6-axis miniature sensor for an implantable hip joint. He holds several international patents in the field of biomechanical indicators and advanced sensor architectures.

Thomas-Martin Schuldt (Member, IEEE) received the diploma degree in Electrical Engineering and Measurement Technology from the Berliner Hochschule für Technik, Berlin, Germany, in 2008. After completing secondary school in Leipzig, Germany, he completed vocational training as an electrician. From 1998 to 2002, he served in the German Armed Forces as a radio operator. In 2004, he received the state-certified technician degree in Electrical Engineering and Communication Technology from the Fachschule für Technik und Wirtschaft Leipzig, Germany. He is currently Head of Electronics Development at ME-Meßsysteme GmbH, Hennigsdorf, Germany. His professional interests include electronic measurement systems, sensor technology, embedded electronics, and industrial communication systems.

Sema Dumanli (Senior Member, IEEE) received the B.Sc. degree in electrical and electronic engineering from METU Ankara, Turkey, in 2006, and the Ph.D. degree from the University of Bristol, Bristol, U.K., in 2010. She conducted research at Toshiba Research Europe, Bristol from 2010 to 2017. She is currently an Associate Professor at Bogazici University, Istanbul. She is the founder of Antennas and Propagation Research Laboratory (BOUNtenna) and Bioelectromagnetics Laboratory (AntennAlive). Her current research interests include antenna design for implantable and wearable devices, in-body sensor design, biohybrid implants, biodegradable sensors, chipless RF-ID sensors and multi-scale communications. Dr Dumanli is the recipient of Science Academy's Young Scientist Award (BAGEP) 2025, the IEEE AP-S Lot Shafai Mid-Career Distinguished Achievement Award 2026, the IEEE APS Donald G. Dudley Jr. Undergraduate Teaching Award 2022, and three times recipient of Boğaziçi University, Faculty of Engineering's Excellence in Teaching Award. She currently serves as the chair of IEEE APS/MTT/EMC/ED Turkey Joint Chapter, the vice-chair of the IEEE APS Young Professionals Committee, and the Associate Editor to IEEE AP-S Digital Communications. Dr Dumanli also serves as a board member and the secretary of URSI Turkey and the chair of URSI Turkey Commission K.